Applied Physics Reviews

RESEARCH ARTICLE | SEPTEMBER 25 2024

Charge self-shuttling triboelectric nanogenerator based on wind-driven pump excitation for harvesting water wave energy

Shijie Liu; Xi Liang ; Jiajia Han; Yuxue Duan; Tao Jiang ; Zhong Lin Wang

Appl. Phys. Rev. 11, 031423 (2024)
https://doi.org/10.1063/5.0225737

Applied Physics Reviews ARTICLE pubs.aip.org/aip/are

Charge self-shuttling triboelectric nanogenerator based on wind-driven pump excitation for harvesting water wave energy

Cite as: Appl. Phys. Rev. **11**, 031423 (2024); doi: 10.1063/5.0225737
Submitted: 26 June 2024 · Accepted: 26 August 2024 ·
Published Online: 25 September 2024

Shijie Liu,[1,2] Xi Liang,[3] Jiajia Han,[1,2] Yuxue Duan,[1,4] Tao Jiang,[1,2,5,a)] and Zhong Lin Wang[1,5,6,a)]

AFFILIATIONS

[1]Beijing Key Laboratory of Micro-Nano Energy and Sensor, Center for High-Entropy Energy and Systems, Beijing Institute of Nanoenergy and Nanosystems, Chinese Academy of Sciences, Beijing 101400, People's Republic of China
[2]School of Nanoscience and Engineering, University of Chinese Academy of Sciences, Beijing 100049, People's Republic of China
[3]The Beijing Key Laboratory for Nano-Photonics and Nano-Structure, Department of Physics, Capital Normal University, Beijing 100048, People's Republic of China
[4]School of Chemistry and Chemical Engineering, Guangxi University, Nanning, Guangxi 530004, People's Republic of China
[5]Guangzhou Institute of Blue Energy, Knowledge City, Huangpu District, Guangzhou 510555, People's Republic of China
[6]Georgia Institute of Technology, Atlanta, Georgia 30332-0245, USA

[a)]Authors to whom correspondence should be addressed: jiangtao@binn.cas.cn and zlwang@gatech.edu

ABSTRACT

The most important ocean energy sources are wind energy and water wave energy, both of which are significant to carbon neutrality. Due to uneven distribution and random movement, the conversion efficiency from the two energies into electrical energy is limited, so the coupling of them is necessary. However, the current energy harvesting technologies generally target one certain type, or are simple mechanical coupling. Here, we propose a composite water wave energy harvesting scheme with wind excitation based on triboelectric nanogenerators (TENGs). A rotation TENG driven by wind is introduced as a pump to inject charges into the main TENG. For the main TENG driven by water waves, a specially designed charge self-shuttling mode is applied (CSS-TENG). Under the pump excitation, the shuttling charge amount is increased by 11.8 times, and the peak power density reaches 33.0 W m^{-3}, with an average power density of 2.4 W m^{-3}. Furthermore, the CSS-TENG is expanded into an array by parallel connection, and the practical applications are demonstrated. This work organically couples the wind and water wave energy in the ocean scene, through the charge pumping and self-shuttling mode, providing a new pathway for the synergistic development of clean and renewable energy sources.

I. INTRODUCTION

Nowadays, the extensive consumption of traditional fossil energy sources has led to a series of problems such as energy storage crises and ecological environment deterioration, thus the vigorous exploitation of renewable energy sources becomes an important topic for humanity.[1–6] Oceans cover over 70% of the earth's surface, containing vast amounts of clean and renewable energy, such as tidal energy,[7] salinity gradient energy,[8] solar energy,[9,10] offshore wind energy,[11–13] and water wave energy.[14–18] Among them, wind energy and water wave energy have immense development potentials due to widespread distribution, abundant reserves, and independence of day–night cycles. At this stage, the collection of offshore wind and water wave energy mostly relies on traditional electromagnetic generators, suffering from large size, high cost, and low efficiency.[19,20] Therefore, developing more effective energy harvesting technologies is urgently needed.

The triboelectric nanogenerator (TENG), first proposed by Wang in 2012, has enormous potential applications in many fields.[21–25] especially in collecting distributed low-frequency and high-entropy energy sources such as wind and water wave energy.[26–32] The working principle of TENGs is based on triboelectrification and electrostatic induction, converting mechanical energy into electrical energy by the Maxwell's displacement current.[33] For traditional TENGs, electrostatic charges are confined entirely on dielectric surfaces, and the low surface charge density limits the output power, severely hindering practical applications. Previous research mainly focused on structural design, material selection, and surface modification to overcome this problem.[34–38] In 2020, Wang first proposed a charge-shuttling TENG, achieving a high charge density of 1.85 $\mathrm{mC\,m^{-2}}$, exhibiting excellent output performance in harvesting water wave energy.[39] However, in this mode, the charge-shuttling conduction domain is restricted between the main TENG and the external buffer capacitor, and the output performance is difficult to improve further.[40,41] Therefore, advanced research on the charge-shuttling mode is still required.

In this work, we designed a high-performance charge self-shuttling TENG (CSS-TENG) for harvesting the water wave energy based on wind-driven pump excitation, in which the charges excited by the pump shuttle inside the CSS-TENG group. In this mode, two symmetrical conduction domains exist due to the mirror flows of the positive and negative charges. According to different circuit connections of the two domains, we distinguished two shuttling types, and compared the outputs, achieving an enhancement of 11.8 times in the transferred charge. Based on the CSS-TENG excited by the wind-driven TENG (WD-TENG), an integrated array device with multiple CSS-TENGs was fabricated to realize the simultaneous harvesting of ocean wind and water wave energy. The conductive domain is between two contact-separation TENGs with completely opposite motion states and variable capacitances, not only expanding the choice of conductive domains under this mode but also avoiding interference between the outputs of TENGs with different motion states. Our work provides a new mode of charge pumping and self-shuttling for TENG devices, offering a new approach for efficient environmental mechanical energy harvesting.

II. RESULTS AND DISCUSSION

A. Structure and working principle of charge self-shuttling TENG based on pump excitation

Figure 1(a) illustrates the application scenario of the charge self-shuttling TENG based on pump excitation. The device consists of a WD-TENG for wind energy collection as the pump TENG and a CSS-TENG for water wave energy collection as the main TENG. Figure 1(b) provides structural details of the two TENGs. The WD-TENG primarily comprises fan blades, a steel shaft, a rotor, and a stator. The rotor is made of an acrylic plate with 8 fan-shaped shallow grooves. Polytetrafluoroethylene (PTFE) and nylon films are alternately adhered to the surface of the acrylic plate. Additionally, the stator is assembled with an acrylic plate as the base, two rows of radial copper foils as induction electrodes, and eight strips of rabbit furs as the triboelectric layer for charge generation. The rabbit furs possess suitable elasticity and softness, and the soft contact keeps an air gap between the rotor and the electrodes, where the coupling of non-contact and soft contact modes can enhance the device durability.

The CSS-TENG, consisting of two external acrylic hemispheres and two internal multilayered spiral hemispheres with thermoplastic polyurethane (TPU) substrates, is optimized based on our previous work. The stiffness coefficient of the TPU substrate is measured to be 48 $\mathrm{N\,m^{-1}}$, behaving like a spring structure capable of storing elastic potential energy. The bottoms of the two substrates are fixed together by a 1 mm thick acrylic plate, ensuring they remain centered within the hemispheres. Two 100 g mass blocks are introduced at the ends of the substrates to alter the center of gravity and enhance the swinging motion. Copper electrodes with a fluorinated ethylene propylene (FEP) film or a nylon film are attached to the upper and lower surfaces of the spring-like substrate. Sufficient internal space allows relative motion between the upper and lower surfaces to facilitate contact and separation of the TENG units. The manufacturing processes of the WD-TENG and CSS-TENG are shown in Fig. S1 (supplementary material). The fabrication details for the two TENGs are provided in the Experimental Section.

The circuit diagram of the charge self-shuttling system based on the pump excitation is illustrated in Fig. 1(c). The system mainly consists of a pump TENG, a main TENG group, a rectifier, and a buffer capacitor. The main TENG group comprises two TENG units with completely opposite motion states, forming two quasi-symmetrical conduction domains (Q^+ side and the Q^- side). The pump TENG injects opposite charges into these two domains through a rectifier, which could withstand high voltage to prevent charge backflow. When two units of the main TENG group alternately contact and separate, the capacitance changes result in voltage differences between the electrodes. The unbalanced voltage further drives charges shuttling across the two loads of the two conduction domains, generating electricity.

The working principle of the main TENG group is illustrated in Fig. 1(d). For simplicity, only the case of the Q^+ side is described here, as the case of the Q^- side is similar. For simplicity, the upper TENG unit corresponds to the left TENG unit in Fig. 1(c), while the lower TENG unit corresponds to the right one. When the upper TENG unit switches to the contacting state, its capacitance increases, causing its voltage drops. Meanwhile, the right TENG unit is in the separating state, leading to the capacitance decrease and voltage rises. When the voltage of the lower unit is higher than the upper unit, charges flow from bottom to top, passing through the load and output electricity until the voltage reaches equilibrium. Subsequently, the upper and lower TENG units reverse movement, and the charges return from top to bottom. Figure 1(e) depicts the electric potential distributions of the two TENG units, using the COMSOL software.

The framework of the composite energy harvesting and application system is depicted in Fig. 1(f). This system consists of three parts: a pump TENG, a main TENG group, and a power management circuit (PMC). The pump TENG and main TENG group are utilized for collecting wind and water wave energy in the environment, integrating the two energies organically and improving the energy utilization efficiency. Subsequently, the PMC is linked with the device to enhance the electrical output and drive the effective operation of backend functional circuits. Finally, the power-managed TENG is employed to power a series of functional circuits, including sensing, display, signal transmission, and so on.

B. Charge self-shuttling mechanism and performance enhancement principle

In order to better understand the charge self-shuttling mechanism of the main TENG group, the most basic two-layer contact-separation TENGs are employed here. A theoretical model without Zener diodes was established, as discussed in detail in Note S1 and Fig. S2. The following equations can briefly describe the TENG outputs:

$$Q_{\mathrm{SC}} = \frac{\dfrac{d_0}{d_0 + x_1(t)} + \dfrac{x(t)}{d_0 + x(t)} + \dfrac{C_{\mathrm{S}} d_0}{S\varepsilon_0}}{d_0\left(1 + \dfrac{C_{\mathrm{S}}}{S\varepsilon_0}\right)} \cdot V_{\mathrm{E}}, \tag{1}$$

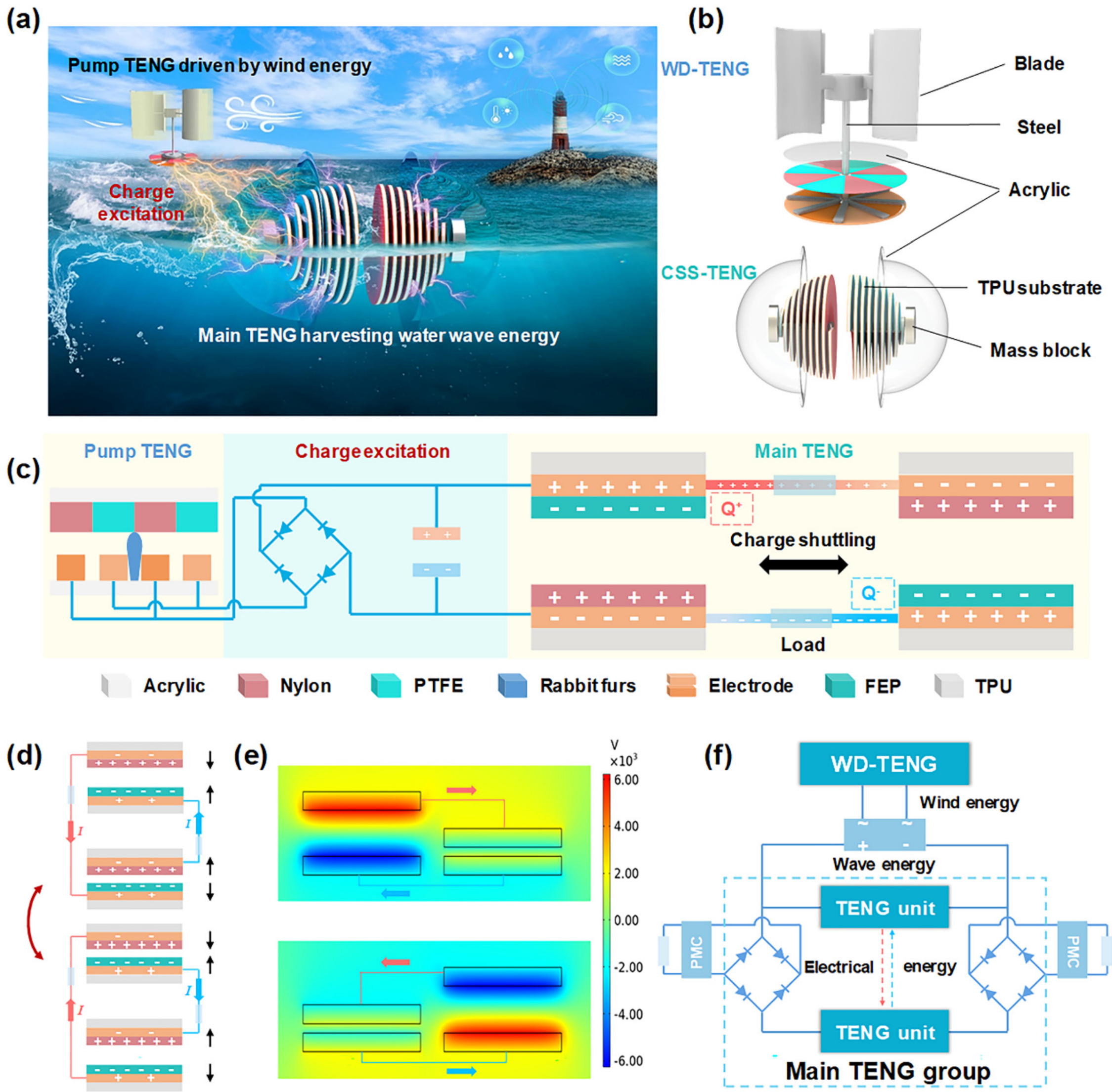

FIG. 1. Design and working principle diagram of the device for harvesting marine multi-energy. (a) Conceptual diagram of the pump-excited TENG for coupling the wind energy and water wave energy harvesting. (b) Schematic structure of the WD-TENG for harvesting wind energy and the CSS-TENG for harvesting water wave energy. (c) Working mechanism of the CSS-TENG with pump excitation. (d) Charge self-shuttling mode inside the main TENG. (e) COMSOL simulation of the voltage potential distribution of the main TENG under different state. (f) Framework diagram of the water wave energy harvesting system based on the wind energy excitation.

$$V_{OC} = \frac{x(t)}{d_0\left[1 + \dfrac{d_0 + x(t)}{d_0 + x_1(t)} + \dfrac{C_S}{S\varepsilon_0}(d_0 + x(t))\right]} \cdot V_E, \tag{2}$$

where Q_{SC} is the shuttled charge amount between the two units of main TENG group under the short-circuit condition, i.e., the short-circuit charge of the main TENG; C_S is the capacitance of the buffer capacitor; V_{OC} and V_E are the open-circuit voltage of the main TENG and the applied pump voltage; d_0 and S are the effective thickness constant and the area of the dielectric layer; $x(t)$ and $x_1(t)$ are the separation distances for the two units at time t; and ε_0 is the permittivity of vacuum.

Then, we discuss the charge self-shuttling mechanism in two cases, including the homogeneous charge self-shuttling (HCSS) and opposite charge self-shuttling (OCSS), as shown in Figs. 2(a) and 2(b). The HCSS refers to the charge conduction domains located between the electrodes attached with homogeneous dielectric materials in the two TENGs, while for the OCSS, the charge conduction domains are between the electrodes attached with heterogeneous dielectric materials. Each mode exhibits two symmetric conduction domains, and the corresponding loads are labeled by loads A, B and loads C, D. Figures 1(d) and 1(e) are about the OCSS mode, while the working principle of the HCSS modes is shown in Fig. S3. To compare the basic output characteristics of these two modes, tests were conducted by using a programmable linear motor at a fixed motion frequency.

First, without the pump TENG, Figs. 2(c) and 2(d) display the transferred charge and output current of the device in the two modes. It is obvious that the transferred charge amounts and current magnitudes at the symmetric loads of one mode are basically identical. The enlarged view in Fig. 2(d) demonstrates perfectly mirrored current curves at the symmetric loads, which is in line with the fundamental output principle of charge shuttling. Comparing different modes, the electrical outputs of load D are slightly higher than load B, but the overall differences are not significant. This indicates that the electrical output of the CSS-TENG primarily depends on the voltage difference between the TENG units. When the capacitance difference in the left and right TENGs is larger, the larger voltage difference will lead to higher electrical output.

Furthermore, we tested the output performances of the main TENG group linked with different buffer capacitors. For simplicity, only one load was selected as the test object for each mode, because the situation for the other load is similar. The comparisons of the transferred charge and output current on loads A and C with different buffer capacitors are shown in Fig. 2(e). Figure S4 presents the specific raw data. The electrical outputs of loads A and C are basically the same as the traditional TENG units, illustrating the output enhancement is limited. Therefore, we introduced the WD-TENG as the

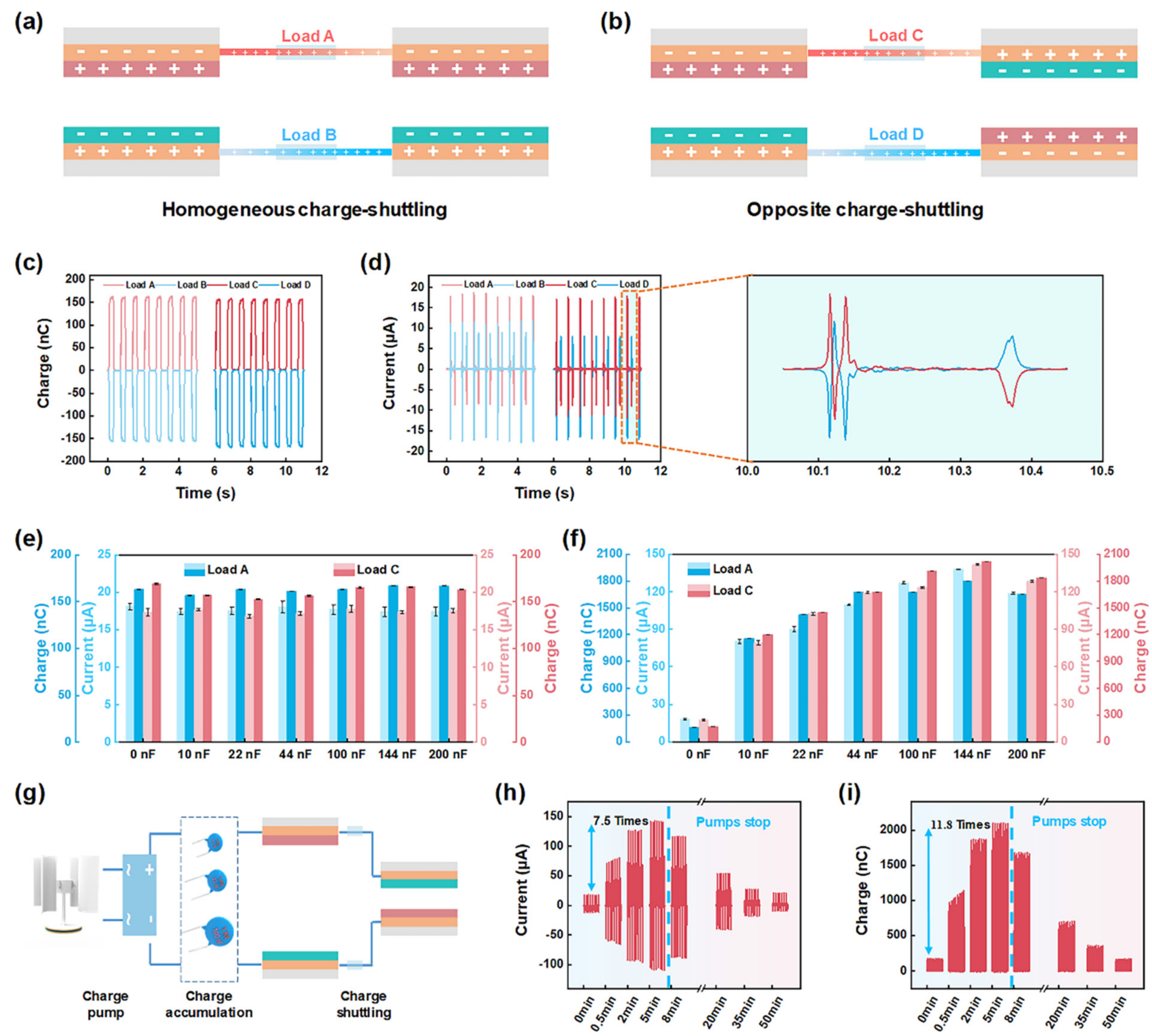

FIG. 2. Working mechanism of the charge self-shuttling mode. (a) and (b) Working diagram of the CS-TENG in the HCSS mode (a) and the OCSS mode (b). (c) and (d) Transferred charge (c) and output current (d) of the CS-TENG in the two modes. (e) and (f) Comparison of transferred charge and output current on different loads with various buffer capacitors, before (e) and after (f) pump excitation. (g) Schematic diagram of pump-excited CS-TENG under various buffer capacitors. (h) and (i) Comparison of output current (h) and transferred charge of the CS-TENG with different excitation times.

charge pump. The WD-TENG serves as the primary charge source to provide charges shuttling inside the main TENG group, as schematically illustrated in Fig. 2(g). Figure 2(f) demonstrates the comparison of the transferred charge and output current on loads A and C with WD-TENG pumping. Figure S5 presents the specific raw data. As the capacitance of the buffer capacitor increases, the output current and transferred charge both first increase and then decrease, so an optimal capacitance exists. When the capacitance of buffer capacitor is small, the excessively high voltage during the TENG separation process results in partial charges being injected into the dielectric layer. Consequently, as the capacitance increases, the transferred charge gradually increases. When the capacitance is too large, the long charging time causes charge dissipation in the system. Therefore, the most matching capacitance for the buffer capacitor exists, which is consistent with the derived results in Note S1.

Since the outputs of the TENGs in the two modes are roughly the same, the OCSS mode was adopted for subsequent experiments. With the optimal buffer capacitor, we tested the output current and transferred charge of the CSS-TENG in a period of time, analyzing the duration of the enhancement effect. As shown in Figs. 2(h) and 2(i), the output current increases from 16.8 to 142.6 μA, with an enhancement of 7.5 times, while the transferred charge increases from 163.6 nC to 2.1 μC by nearly 11.8 times. Moreover, when the pump TENG is continuously operating, it pumps a large amount of charges into the conductive domain of the main TENG group. Even after the pump TENG stops, the pumped charges do not immediately disappear but continue to shuttle back and forth in the conductive domain with the capacitance change at both ends of the TENGs, resulting in energy outputs in the external circuit. When the pump TENG is stopped for 45 min, the charges eventually dissipate completely due to the energy loss, and the outputs return to the initial state, which demonstrates the potential application of the pump-excited charge self-shuttling mode in practical environments.

C. Output characteristics of WD-TENG and pump-excited CSS-TENG

The CSS-TENG based on the pump excitation provides a promising route toward environmental energy harvesting. Here, a high-performance integrated CSS-TENG device for simultaneous harvesting ocean wind energy and water wave energy was fabricated. The pump WD-TENG collects wind energy, while the main CSS-TENG with the multilayered spiral hemisphere structure collects the water wave energy. The WD-TENG with high voltage and durability can continuously and steadily pump charges to the conduction domain of the main TENG group. To reveal the influence of the wind speed, the output current, transferred charge, and output voltage of the WD-TENG were measured, as shown in Figs. 3(a)–3(c). It can be seen that as the wind speed increases, the output current increases from 2.0 to 4.5 μA, because the current is related to the relative velocity between the rotor and the stator. The output voltage increases from 663 to 952 V, while the transferred charge remains essentially unchanged. The number of grids is fixed, and the distance between the rotor and the stator is 3 mm, but the rotor is point-fixed to the bearing and is not completely horizontal due to its gravity, causing the rotor–stator distance to fluctuate around 3 mm. As the operating frequency increases, the rotational speed of the rotor increases, causing more pronounced fluctuations in the rotor–stator distance. This results in enhanced electrostatic induction between the dielectric film in the rotor and the electrode in the stator, leading to a slight increase in the voltage of pump TENG. All the results are in line with the basic output characteristics of TENGs. In order to closely match the real marine environment, we found that in most oceans around the world, the wind power density exceeds 50.0 W m^{-2} for 80% of the year. Based on this, we selected a standard test wind speed of 4.3 m s^{-1} for driving the WD-TENG (Fig. S6 and Note S2).

Subsequently, we studied the effect of working frequency on the output performance of a multilayered hemispherical TENG unit (half of the spherical TENG), at a fixed motion distance of 20 mm. In Figs. 3(d), 3(e), and S7(a), the trends of the output current, transferred charge, and output voltage are shown as the frequency increases from 0.5 to 2.5 Hz. It is observed that the transferred charge of 586.0 nC and the output voltage of 344 V remain unchanged, while the output current increases from 2.1 to 11.1 μA.

Next, we tested the output performance of the whole spherical TENG based on the pump-excited CSS mode at the frequency of 1 Hz. For simplicity, we only demonstrate the electrical outputs of one domain, as the other domain is similar (Fig. S8). Using Zener diodes to avoid electrostatic breakdown, the output current, transferred charge, and output voltage gradually increase with the charge pumping until saturation, as shown in Figs. 3(f), 3(g), and S7(b). From Fig. 3(g) and its inset, the transferred charge increases up to 2.5 μC and remains stable for a long time, exhibiting a 3.3 times increase compared to the traditional mode. Figure S9 shows that without Zener diodes, the transferred charge can reach about 4.0 μC, with a peak power density of 33.0 W m^{-3} and an average power density of 2.4 W m^{-3}, indicating Zener diodes causes some energy loss in the domain.

To further validate the high performance of the CSS-TENG, two 100 μF capacitors were simultaneously charged by two conduction domains at the frequency of 1 Hz, and the charging voltages arrive at 0.22 and 0.23 V within 15 s [Fig. 3(h)], implying that the outputs can be used for powering electronic devices. Figure S10 illustrates the specific charging circuit. Then, we compared the charging capability of one conduction domain with or without the pump excitation, as shown in Fig. 3(i). In 15 s, the 100 μF capacitor is charged to 0.92 V with the pump TENG, and the stored energy is 16.5 times higher than the case without the pump TENG. The results indicate that the pump-excited CSS-TENG device can provide higher outputs for mechanical energy harvesting.

D. Applications of pump-excited CSS-TENG array for water wave energy harvesting

To investigate the output performance of the pump-excited CSS-TENG device in real water waves, the fabricated device was tested in a simulated wave tank. Before measurements, the device was sealed and waterproofed with polymer glues to prevent the negative effects of moisture. The water wave conditions were fixed at the frequency of 0.8 Hz and the height of 9 cm, while the experimental wind speed was fixed at 4.3 m s^{-1}. An array device consisting of several multilayered helical TENGs (MH-TENGs) was constructed through the parallel electrical connection to enhance the water wave energy harvesting scale, as schematically shown in Fig. 4(a). In the TENG array, we directly connected the electrodes of TENG units in parallel, and only the overall final output terminal was connected to a rectifier bridge, converting the alternating current (AC) into the direct current (DC).

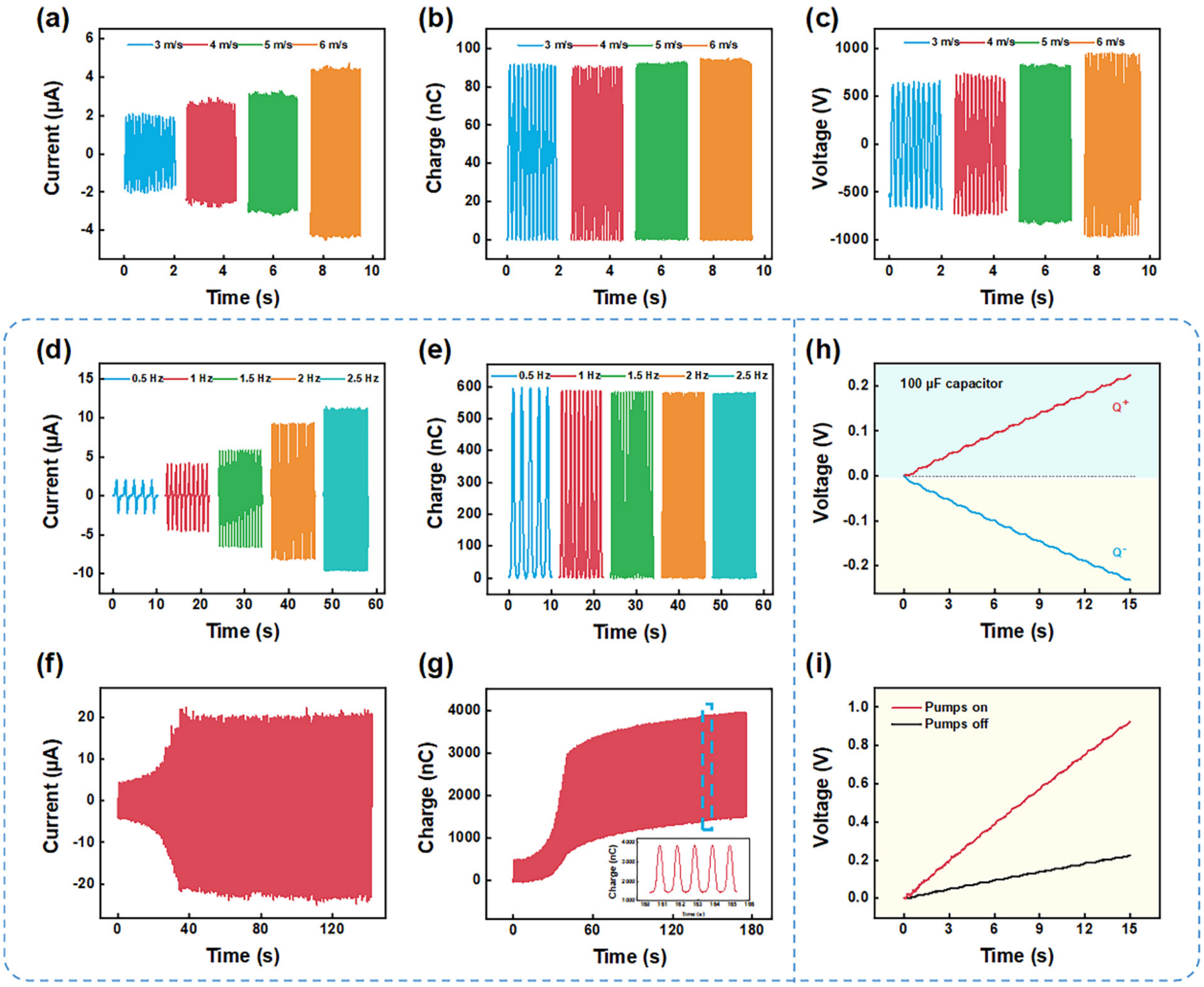

FIG. 3. Electrical performance of the WD-TENG and the CSS-TENG. (a)–(c) Output current (a), transferred charge (b) and output voltage (c) of the WD-TENG at various wind speeds. (d)and (e) Output current and (d) transferred charge (e) of the semispherical TENG unit triggered by the linear motor at various frequencies. (f) and (g) Output current (f) and transferred charge (g) at one output terminal of the CSS-TENG with pump excitation. (h) Voltage curves of two capacitors at the two output terminals charged by the CSS-TENG simultaneously without pump excitation. (i) Charging voltage curves of a 100 μF capacitor at one output terminal of the CSS-TENG with or without pump excitation.

This method eliminated the need for each TENG unit to be connected to a rectifier bridge, simplifying the wiring of the array, and reducing the energy loss.

Then, the influence of the TENG unit number in the array on the electrical outputs was evaluated, as shown in Figs. 4(b) and 4(c). Regarding the output current, the peak values gradually increase with increasing the unit number, reaching 103.2 μA for 4 units. For the peak voltage, the value remains around 320 V, and the signal density increases due to the parallel connections. Figure 4(d) shows the charging performance of the TENG array with different unit numbers (the capacitor is 100 μF). It can be seen that more units result in faster charging speed, where the 4-unit TENG array can charge the capacitor to 0.65 V in 15 s. In addition, the resistive output behavior of the CSS-TENG array was investigated. As presented in Fig. 4(e), the peak current and voltage, respectively, decreases and increases with the increasing resistance. The 4-unit CSS-TENG array can deliver a maximum peak power of 29.1 mW and a maximum average power of 1.4 mW at the matched resistance of 22 MΩ [Fig. 4(f)]. The corresponding peak power density is 13.9 W m^{-3} and average power density is 0.7 W m^{-3}. Based on this, we can determine that the energy conversion efficiency of the CSS-TENG array under periodic wave excitation is 9.11% (Note S3). For each CSS-TENG unit in the array, the maximum peak power density decreases because of the indirect perturbation between the multiple units. Then, the 4-unit array is integrated with a PMC, and the typical charging voltage profiles to various load capacitors from 47 to 1000 μF are shown in Fig. 4(g). Under water waves, the voltage on the 100 μF capacitor can increase from 0 to 2.20 V in 15 s. The outstanding performance verifies that the integration of multiple CSS-TENG units is a promising solution for large-scale water wave energy harvesting.

For practical applications, the CSS-TENG array with the WD-TENG pump excitation was integrated with a PMC to realize the

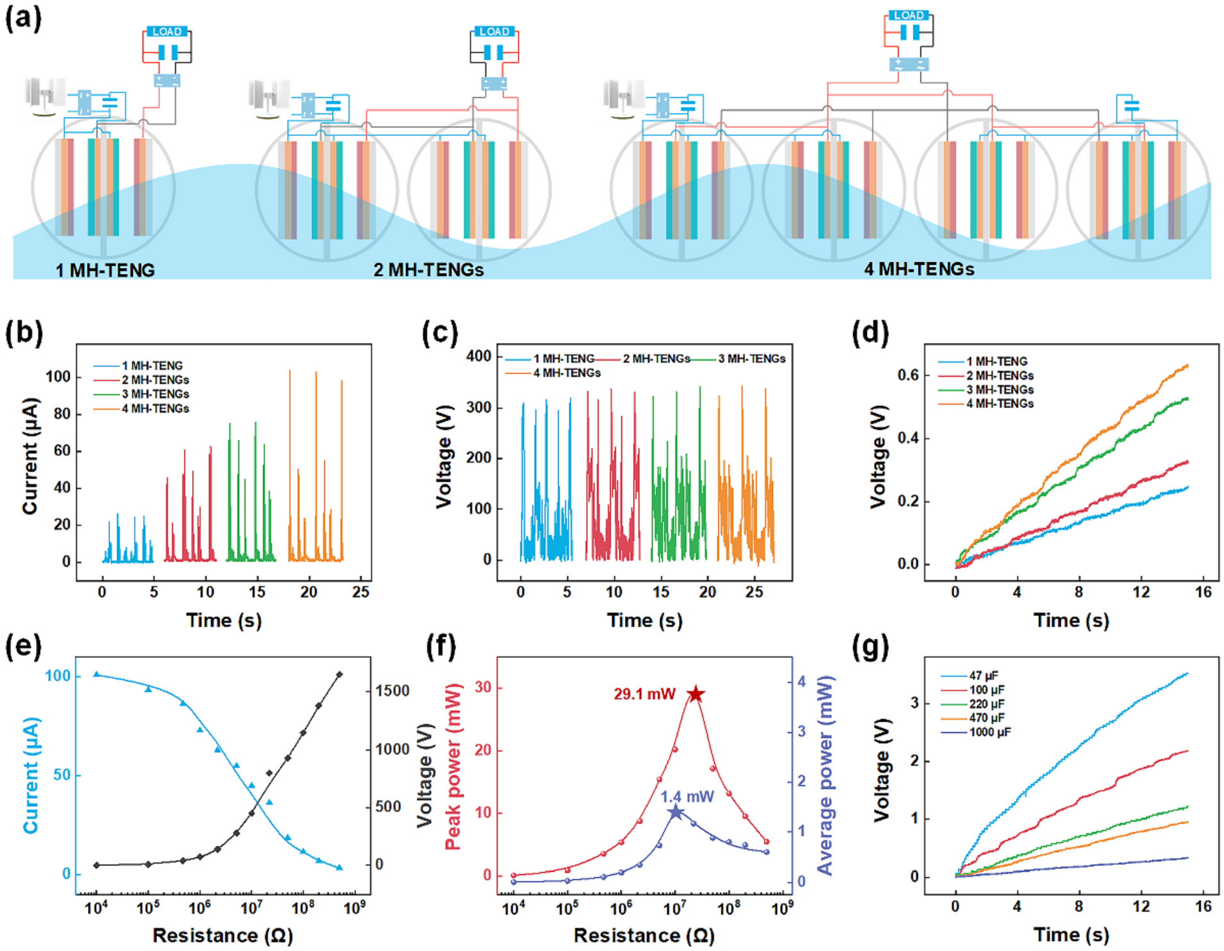

FIG. 4. Output performance of pump-excited CSS-TENG array for water wave energy harvesting. (a) Schematic diagram of the CSS-TENG array with multiple units under the water wave condition. (b) and (c) Output current (b), output voltage (c) of the CSS-TENG array with different unit numbers. (d) Charging speed comparison of the CSS-TENG array with different unit numbers. (e) and (f) Peak current and voltage (e), peak power and average power (f) of the 4-unit CSS-TENG array under various load resistances. (g) Charging voltage profiles of the 4-unit CSS-TENG array with the PMC for various capacitors. The agitation frequency is 0.8 Hz.

simultaneous harvesting of wind and water wave energy toward ocean-related self-powered systems. Figure 5(a) shows the schematic diagram of the system containing the pump WD-TENG as the wind energy collector, the CSS-TENG array as a water wave energy collector, a full-wave rectifier bridge, a PMC, a backend energy storage element, and application loads. The rectifier bridge consists of 4 high-voltage diodes. Here, a PMC based on a buck module is employed, which can be divided into buck and regulation parts. The voltage-controlled switch in the buck part is composed of a breakdown diode D_1 and a silicon-controlled rectifier (SCR, EC103M1). The positive pole of D_1 is connected to the gate of the SCR, and a parallel resistor can be chosen based on the leakage current of D_1. The regulation part consists of an inductor L, a capacitor C_{out}, and a regular diode D_2. When C_{in} is charged to a voltage greater than the breakdown voltage of D_1, the current on D_1 triggers the SCR to conduct, until the charges stored in C_{in} flows into L. In the next stage, the current oscillates through the loop of L, C_{out}, and D_2, and the voltage on C_{out} gradually increases to power loads.

To demonstrate the capability of the pump-excited CSS-TENG array as a power source for applications, several examples about the environmental information detection were conducted. Unless otherwise stated, the water wave conditions were fixed at a wave frequency of 0.8 Hz and a wave height of 9 cm. As shown in Fig. 5(b), in order to meet the power requirements, the TENG array first charges a capacitor of 1 mF to convert pulse outputs into constant outputs. Once the voltage on the capacitor rises to 5.00 V, the switch is on to power the anemometer. Utilizing this constant DC power, the anemometer can autonomously measure wind speed information and display real-time values on the LCD screen (Video S1). Figure 5(c) shows the voltage curve on the capacitor of 2.2 mF to power the humidity and temperature sensor. When the charging voltage rises to 3.50 V, the humidity and temperature sensor starts working and detecting the environment temperature and humidity. The experimental process was recorded in Video S2. Additionally, the device can keep 240 light-emitting diodes (LEDs) with the diameter of 10 mm continuously illuminated (Video S3). The typical voltage curve on the capacitor (3.3 mF) during the

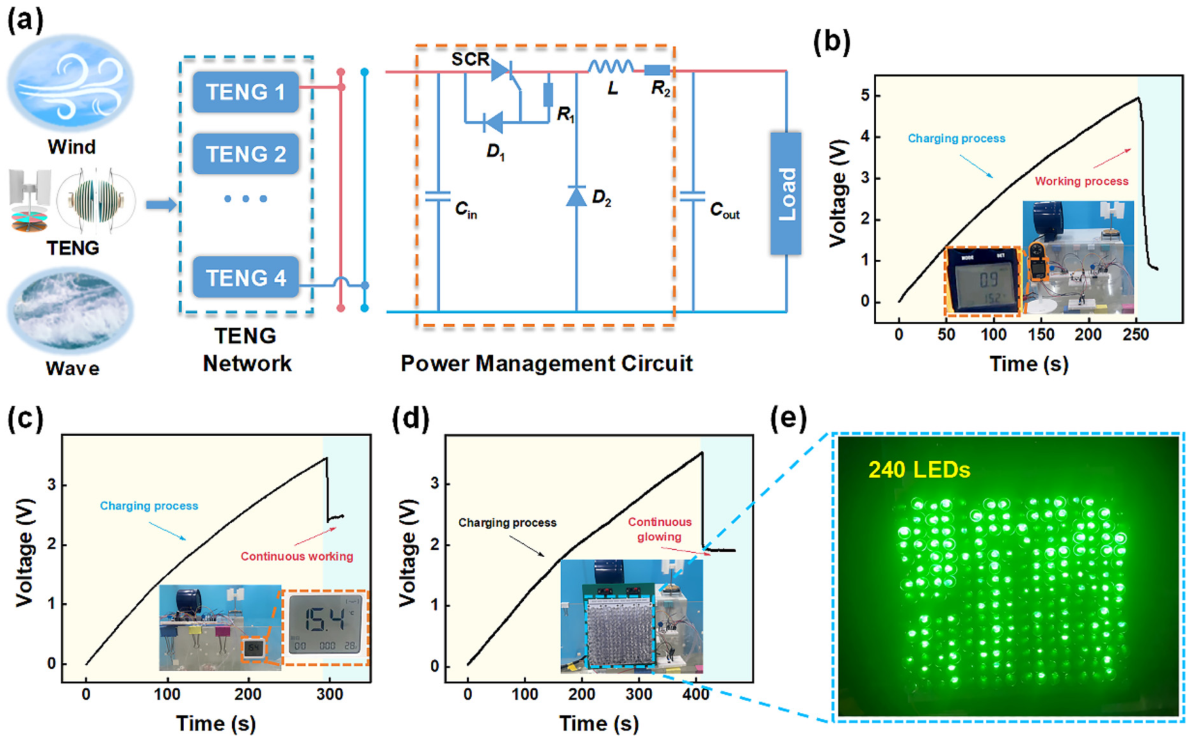

FIG. 5. Demonstration and applications of the pump-excited CSS-TENG Array. (a) Schematic diagram of the pump-excited CSS-TENG array integrated with the PMC. (b) and (c) Voltage profiles on the wind speed sensor (b) and the commercial temperature and humidity sensor (c) powered by the CSS-TENG array. (d) and (e) Application demonstration for the CSS-TENG array powering 240 LEDs (the diameter of one LED is 10 mm). The voltage profile (d) on the LEDs and the photograph (e) of the lighted LEDs are shown.

charging and discharging process is shown in Fig. 5(d). It can be observed that the LEDs are lit up when the voltage on the capacitor reaches 3.50 V. Subsequently, the voltage on the capacitor remains stable, and the LEDs are constantly illuminated. The above data demonstrate the feasibility and practicality of the pump-excited CSS-TENG array for energy harvesting and application in the ocean.

III. CONCLUSION

In summary, a charge self-shuttling TENG device integrated with pump excitation was proposed. Unlike previous charge-shuttling modes between the TENG and external buffer capacitor, the CSS-TENG has symmetric conduction domains inside the main TENG group. Not only that, the pump TENG injects more charges into the CSS-TENG group, improving the output performance. An enhancement of transferred charge by 11.8 times was achieved. Then, the complete device based on the special working mode was constructed for simultaneously collecting wind and wave energy, with the peak power density of 33.0 W m^{-3} and the average power density of 2.4 W m^{-3}. Furthermore, several CSS-TENG units were arrayed with simplified wiring and low energy loss to improve the energy harvesting scale. The applications of a wind speed sensor, a thermo-hygrometer, and an LED array were demonstrated. In this work, the wind and water wave energy harvesting was organically integrated by the pump-excited CSS-TENG, showing significant practical value in the fields of self-powered systems and blue energy.

IV. EXPERIMENTAL SECTION

A. Fabrication of devices

Fabrication of the basic contact-separation TENG: Two acrylic boards were cut into $100 \times 100 \times 5\ mm^3$ using a laser cutting machine (PLS6.75). A high-density foam ($100 \times 100 \times 3\ mm^3$) was introduced onto the upper surface of each acrylic board as a cushioning layer. A 30 μm thick FEP film was attached to a copper electrode (100 mm $\times$ 100 mm $\times$ 20 μm) on one board. A 25 μm thick nylon film was attached to another copper electrode on the other board.

Fabrication of the spherical CSS-TENG: Initially, two hemispherical substrates were 3D printed using TPU materials within a spherical shell. Each substrate has a diameter of 100 mm, a thickness of 3 mm, a height of 50 mm, and nine spring coils. The physical and mechanical properties of the S-TPU printed structure are as follows: density of 1.2 g cm^{-3}, Shore hardness of 88 A, Poisson's ratio of 0.45, tensile strength of 20 MPa, elongation at break of 600%, compressive strength of 43.5 MPa, compressive modulus of 15.9 MPa, over 50 000 bending cycles, and melting temperature of 160 °C. Then, two 20 μm thick copper foils were then affixed to the upper and lower surfaces of each substrate, applying 30 μm thick FEP films and 25 μm thick nylon films as dielectric layers. The two units were integrated into a 10 cm diameter sphere inside an acrylic shell, with two mass blocks assembled on top of each substrate, forming a complete CSS-TENG. To mitigate humidity-related issues, waterproofing was applied using polymer glues, ensuring sustained electrical performance over time.

Fabrication of the WD-TENG: The WD-TENG consists of three components: a stator, a rotor, and fan blades. The stator was made from a 5 mm thick acrylic circular board with an outer diameter of 100 mm and an inner diameter of 10 mm. Radial holes and shallow grooves, with central angles of 6° and 39°, respectively, were made on its surface using a laser cutting machine. Copper foil electrodes, with a thickness of 20 μm, were attached to the stator surface, and rabbit furs were mounted through the holes. The rotor, made from a 3 mm thick acrylic board with the similar shape, features eight shallow grooves engraved on its surface with a rotation angle of 45°. PTFE and nylon films were alternately attached to the rotor surface and cut along the grooves. The fan blades, designed using SolidWorks software, were 3D printed with the height of 90 mm and the arc length of 57.5 mm. The fan blades drive the rotor to rotate through a fixed plate and steel shaft.

B. Electrical characterizations of the devices

The electrical performance of the WD-TENG was measured under ideal triggering conditions generated by a variable frequency ducted fan (SE-A200). The wind speed was determined using a standard anemometer (AS836). The electrical outputs of the spherical CSS-TENG device were measured under ideal triggering conditions generated by a linear motor (LINMOT 1100), or under water wave conditions generated by a standard wave tank as previously reported. The wave tank includes a wave-making mechanism and rebound wave absorbers. The output current, transferred charge, output voltage of all TENGs, and charging voltage curves were measured by a current pre-amplifier (Keithley 6514 System Electrometer, using a high-voltage attenuation probe HVP-40).

SUPPLEMENTARY MATERIAL

See the supplementary material data to this article, which can be found online.

ACKNOWLEDGMENTS

The research was supported by the National Key R & D Project from the Minister of Science and Technology (Nos. 2021YFA1201604 and 2021YFA1201601), the Beijing Nova Program (No. 20220484036), the Innovation Project of Ocean Science and Technology (No. 22-3-3-hygg-18-hy), the China National Postdoctoral Program for Innovative Talents (No. BX20230357), and the Youth Innovation Promotion Association, CAS.

AUTHOR DECLARATIONS

Conflict of Interest

The authors have no conflicts to disclose.

Author Contributions

Shijie Liu, Xi Liang, and Jiajia Han contributed equally to this work.

Shijie Liu: Conceptualization (equal); Investigation (equal); Methodology (equal); Writing – original draft (equal). **Xi Liang:** Investigation (lead); Writing – original draft (lead). **Jiajia Han:** Investigation (lead); Visualization (lead). **Yuxue Duan:** Investigation (supporting); Methodology (equal). **Tao Jiang:** Investigation (equal); Supervision (equal); Writing – review & editing (equal). **Zhonglin Wang:** Supervision (lead); Writing – review & editing (lead).

DATA AVAILABILITY

The data that support the findings of this study are available from the corresponding authors upon reasonable request.

REFERENCES

[1]S. Chu and A. Majumdar, "Opportunities and challenges for a sustainable energy future," Nature **488**(7411), 294–303 (2012).
[2]J. Scruggs and P. Jacob, "Harvesting ocean wave energy," Science **323**, 1176–1178 (2009).
[3]J. Tollefson, "Power from the oceans: Blue energy," Nature **508**, 302–304 (2014).
[4]O. Ellabban, H. Abu-Rub, and F. Blaabjerg, "Renewable energy resources: Current status, future prospects and their enabling technology," Renewable Sustainable Energy Rev. **39**, 748–764 (2014).
[5]H. L. van Soest, M. G. J. den Elzen, and D. P. van Vuuren, "Net-zero emission targets for major emitting countries consistent with the Paris agreement," Nat. Commun. **12**(1), 2104 (2021).
[6]S. Hajra, A. Ali, S. Panda, H. W. Song, P. M. Rajaitha, D. Dubal, A. Borras, P. In-Na, N. Vittayakorn, V. Vivekananthan, H. J. Kim, S. Divya, and T. H. Oh, "Synergistic integration of nanogenerators and solar cells: Advanced hybrid structures and applications," Adv. Energy Mater. **14**(21), 2400025 (2024).
[7]C. Shetty and A. Priyam, "A review on tidal energy technologies," Mater. Today: Proc. **56**, 2774–2779 (2022).
[8]N. Y. Yip, D. Brogioli, H. V. M. Hamelers, and K. Nijmeijer, "Salinity gradients for sustainable energy: Primer, progress, and prospects," Environ. Sci. Technol. **50**(22), 12072–12094 (2016).
[9]N. S. Lewis, "Toward cost-effective solar energy use," Science **315**(5813), 798–801 (2007).
[10]D. J. Burke and D. J. Lipomi, "Green chemistry for organic solar cells," Energy Environ. Sci. **6**(7), 2053–2066 (2013).
[11]R. Saidur, M. R. Islam, N. A. Rahim, and K. H. Solangi, "A review on global wind energy policy," Renewable Sustainable Energy Rev. **14**(7), 1744–1762 (2010).
[12]C. W. Zheng and J. Pan, "Assessment of the global ocean wind energy resource," Renewable Sustainable Energy Rev. **33**, 382–391 (2014).
[13]C. W. Zheng, C. Y. Li, J. Pan, M. Y. Liu, and L. L. Xia, "An overview of global ocean wind energy resource evaluations," Renewable Sustainable Energy Rev. **53**, 1240–1251 (2016).
[14]S. H. Salter, "Wave power," Nature **249**(5459), 720–724 (1974).
[15]J. D. Isaacs and W. R. Schmitt, "Ocean energy: Forms and prospects," Science **207**, 265 (1980).
[16]Z. L. Wang, "Catch wave power in floating nets," Nature **542**(7640), 159–160 (2017).
[17]S. Panda, S. Hajra, Y. Oh, W. Oh, J. H. Y. Lee, H. Shin, V. Vivekananthan, Y. Yang, Y. K. Mishra, and H. J. Kim, "Hybrid nanogenerators for ocean energy harvesting: Mechanisms, designs, and applications," Small **19**(25), 2300847 (2023).
[18]Q. Xu, C. Shang, H. Ma, Q. Hong, C. Li, S. Ding, L. Xue, X. Sun, Y. Pan, T. Sugahara, Y. Yalikun, Y.-C. Lai, and Y. Yang, "A guided-liquid-based hybrid triboelectric nanogenerator for omnidirectional and high-performance ocean wave energy harvesting," Nano Energy **109**, 108240 (2023).
[19]A. F. d. O. Falcão, "Wave energy utilization: A review of the technologies," Renewable Sustainable Energy Rev. **14**(3), 899–918 (2010).
[20]H. Hong, X. Yang, H. Cui, D. Zheng, H. Wen, R. Huang, L. Liu, J. Duan, and Q. Tang, "Self-powered seesaw structured spherical buoys based on a hybrid triboelectric–electromagnetic nanogenerator for sea surface wireless positioning," Energy Environ. Sci. **15**(2), 621–632 (2022).
[21]F. R. Fan, Z. Q. Tian, and Z. L. Wang, "Flexible triboelectric generator!," Nano Energy **1**(2), 328–334 (2012).

[22] Z. L. Wang, J. Chen, and L. Lin, "Progress in triboelectric nanogenerators as a new energy technology and self-powered sensors," Energy Environ. Sci. **8**(8), 2250–2282 (2015).
[23] C. Wu, A. C. Wang, W. Ding, H. Guo, and Z. L. Wang, "Triboelectric nanogenerator: A foundation of the energy for the new era," Adv. Energy Mater. **9**(1), 1802906 (2018).
[24] H. Zhao, M. Xu, M. Shu, J. An, W. Ding, X. Liu, S. Wang, C. Zhao, H. Yu, H. Wang, C. Wang, X. Fu, X. Pan, G. Xie, and Z. L. Wang, "Underwater wireless communication via TENG-generated Maxwell's displacement current," Nat. Commun. **13**(1), 3325 (2022).
[25] Y. C. Pan, Z. Dai, H. Ma, J. Zheng, J. Leng, C. Xie, Y. Yuan, W. Yang, Y. Yalikun, X. Song, C. B. Han, C. Shang, and Y. Yang, "Self-powered and speed-adjustable sensor for abyssal ocean current measurements based on triboelectric nanogenerators," Nat. Commun. **15**, 6133 (2024).
[26] J. Han, Y. Feng, P. Chen, X. Liang, H. Pang, T. Jiang, and Z. L. Wang, "Wind-driven soft-contact rotary triboelectric nanogenerator based on rabbit fur with high performance and durability for smart farming," Adv. Funct. Mater. **32**(2), 2108580 (2021).
[27] L. N. Y. Cao, E. R. Su, Z. J. Xu, and Z. L. Wang, "Fully enclosed microbeads structured TENG arrays for omnidirectional wind energy harvesting with a portable galloping oscillator," Mater. Today. **71**, 9–21 (2023).
[28] C. Zhang, L. He, L. Zhou, O. Yang, W. Yuan, X. Wei, Y. Liu, L. Lu, J. Wang, and Z. L. Wang, "Active resonance triboelectric nanogenerator for harvesting omnidirectional water-wave energy," Joule **5**(6), 1613–1623 (2021).
[29] X. Liang, S. J. Liu, Z. W. Ren, T. Jiang, and Z. L. Wang, "Self-powered intelligent buoy based on triboelectric nanogenerator for water level alarming," Adv. Funct. Mater. **32**(35), 2205313 (2022).
[30] S. J. Liu, X. Liang, P. F. Chen, H. R. Long, T. Jiang, and Z. L. Wang, "Multilayered helical spherical triboelectric nanogenerator with charge shuttling for water wave energy harvesting," Small Methods **7**(3), 2201392 (2023).
[31] Y. X. Duan, H. X. Xu, S. J. Liu, P. F. Chen, X. Y. Wang, L. Xu, T. Jiang, and Z. L. Wang, "Scalable rolling-structured triboelectric nanogenerator with high power density for water wave energy harvesting toward marine environmental monitoring," Nano Res. **16**(9), 11646–11652 (2023).
[32] X. Wang, C. Ye, P. Chen, H. Pang, C. Wei, Y. Duan, T. Jiang, and Z. L. Wang, "Achieving high power density and durability of multilayered swing-structured triboelectric nanogenerator toward marine environmental protection," Adv. Funct. Mater. **34**(6), 2311196 (2023).
[33] Z. L. Wang, "On Maxwell's displacement current for energy and sensors: The origin of nanogenerators," Mater. Today **20**(2), 74–82 (2017).
[34] Q. Y. Li, W. L. Liu, H. M. Yang, W. C. He, L. Long, M. B. Wu, X. M. Zhang, Y. Xi, C. G. Hu, and Z. L. Wang, "Ultra-stability high-voltage triboelectric nanogenerator designed by ternary dielectric triboelectrification with partial soft-contact and non-contact mode," Nano Energy **90**, 106585 (2021).
[35] X. Liang, S. Liu, S. Lin, H. Yang, T. Jiang, and Z. L. Wang, "Liquid–solid triboelectric nanogenerator arrays based on dynamic electric-double-layer for harvesting water wave energy," Adv. Energy Mater. **13**(24), 2300571 (2023).
[36] D. Wang, X.-X. Wang, M. L. Jin, P. He, and S. Zhang, "Molecular level manipulation of charge density for solid-liquid TENG system by proton irradiation," Nano Energy **103**, 107819 (2022).
[37] X. Y. Li, L. Xu, P. Lin, X. D. Yang, H. M. Wang, H. F. Qin, and Z. L. Wang, "Three-dimensional chiral networks of triboelectric nanogenerators inspired by metamaterial's structure," Energy Environ. Sci. **16**(7), 3040–3052 (2023).
[38] B. Nowacki, K. Mistewicz, S. Hajra, and H. J. Kim, "3D printed triboelectric nanogenerator for underwater ultrasonic sensing," Ultrasonics **133**, 107045 (2023).
[39] H. M. Wang, L. Xu, Y. Bai, and Z. L. Wang, "Pumping up the charge density of a triboelectric nanogenerator by charge-shuttling," Nat. Commun. **11**(1), 4203 (2020).
[40] W. L. Liu, Z. Wang, G. Wang, G. L. Liu, J. Chen, X. J. Pu, Y. Xi, X. Wang, H. Y. Guo, C. G. Hu, and Z. L. Wang, "Integrated charge excitation triboelectric nanogenerator," Nat. Commun. **10**(1), 1426 (2019).
[41] Z. Yang, Y. Yang, H. Wang, F. Liu, Y. Lu, L. Ji, Z. L. Wang, and J. Cheng, "Charge pumping for sliding-mode triboelectric nanogenerator with voltage stabilization and boosted current," Adv. Energy Mater. **11**(28), 2101147 (2021).